Surfaces and Interfaces 86 (2026) 108792

Contents lists available at ScienceDirect

Surfaces and Interfaces

journal homepage: www.sciencedirect.com/journal/surfaces-and-interfaces

Glycosylated β-C_3N_4 carbon nanodots for warburg effect-driven photothermal therapy of tumors

Roberta Cillari [a], Alice Sciortino [b], Radian Popescu [c], Riccardo Rubino [b], Yolita M. Eggeler [c], Marco Cannas [b], Fabrizio Messina [b], Gennara Cavallaro [a], Nicolò Mauro [a,*]

[a] Department of "Scienze e Tecnologie Biologiche, Chimiche e Farmaceutiche" (STEBICEF), University of Palermo, Via Archirafi 32, 90123 Palermo, Italy
[b] Dipartimento di Fisica e Chimica – Emilio Segrè, Università degli Studi di Palermo, Via Archirafi 36, 90123 Palermo, Italy
[c] Laboratory for Electron Microscopy, Karlsruhe Institute of Technology|KIT, Finanzmanagement Kaiserstraße 12, D-76131 Karlsruhe, Germany

ARTICLE INFO

Keywords:
Carbon nanodots
Photothermal therapy
Fluorescence imaging
Breast cancer
Targeted therapy

ABSTRACT

Harnessing self-trackable nanomaterials capable of converting light into heat for cancer photothermal therapy (PTT) offers a non-invasive, selective, and tunable therapeutic approach in precision medicine. However, successful clinical translation of theranostic agents for image-guided cancer PTT requires proving safety, efficacy, scalable production, and strong tumor targeting driven by metabolic activity or receptor binding. Here, we report a comprehensive evaluation of homogeneous carbon nanodots with β-C_3N_4 crystalline structure, tunable multicolor fluorescence, high cytocompatibility, and efficient photothermal conversion as a theranostic nanoplatform for PTT applications. Optimizing the irradiation parameters to selectively reach mild-hyperthermia conditions (42–49 °C), we achieved controlled antitumoral effects in triple-negative breast cancer cells. The developed nanoheater was further conjugated with 2-deoxy- or 6-deoxy-D-glucose to enhance tumor targeting via GLUT1-mediated uptake, leveraging the abnormal glucose metabolism of cancer cells (Warburg effect). Glycosylation did not compromise CDs' optical properties, resulting in a nanostructure with ideal physical characteristics for PTT applications. *In vitro* assays on 2D and 3D models validated the active targeting strategy adopted and the photothermal efficacy of the nanosystems, also emphasizing a superior performance for CDs-6-Glu with respect to CDs-2-Glu. Altogether, this study aims to advance the development of safer, bioeliminable, more selective, and precisely controllable photothermal therapies through the rational design of glycosylated carbon nanodots tailored for targeted cancer treatment.

1. Introduction

Photothermal therapy (PTT) has demonstrated huge potential to achieve non-invasive, modulable, and selective anticancer treatments [1,2]. This therapeutic strategy uses nanomaterials capable of converting the absorbed light into heat to induce a localized temperature rise at the tumor site, with clinical outcome strongly dependent on the temperature range reached. Specifically, thermal treatments that raise temperatures to mild hyperthermia levels (42–49 °C) specifically target cancer cells by triggering controlled cell death mechanisms and enhancing sensitivity to concurrent therapies. In contrast, temperatures above 49 °C result in tumor ablation through necrosis of the targeted tissues [3–5].

Compared to conventional clinical approaches such as laser ablation or loco-regional hyperthermia [5–7], the application of nanoheaters enables non-invasive precise spatial confinement and fine-tuned control of temperature rise, achieved by optimizing key irradiation parameters, such as photothermal agent concentration, laser power density, and exposure duration, to induce specific and reproducible biological responses [8–10]. Although various nanotechnologies have been proposed, such as gold nanorods [11], modified graphene [12], carbon nanotubes [13], and metal-organic frameworks [14], carbon nanodots (CDs) have attracted significant attention as promising photothermal agents. They offer a less toxic, more environmentally friendly, and cost-effective alternative to traditional nanotechnologies commonly used for this purpose [15,16].

Upon excitation, CDs can relax to the ground state via radiative emission and non-radiative pathways, for instance through energy

* Corresponding author.
E-mail address: nicolo.mauro@unipa.it (N. Mauro).

https://doi.org/10.1016/j.surfin.2026.108792
Received 6 November 2025; Received in revised form 3 February 2026; Accepted 13 February 2026
Available online 14 February 2026

transfer or ultimately resulting in energy dissipation in the form of heat [17]. While the latter efficiently enables PTT, the fluorescence emission of CDs enables high-resolution monitoring of NPs localization, also at sub-cellular level, conferring theranostic features to these nanoparticles and providing significant spatiotemporal control of the antitumoral treatment [18–21]. The intriguing optical properties of CDs are further supported by many advantageous properties such as high-water solubility, ease of synthesis, quasi-zero dimensions, and a large specific surface area enriched with reactive functional groups [22].

The versatile surface chemistry of carbon dots (CDs) enables efficient functionalization with targeting moieties [23,24], facilitating active targeting strategies that promote preferential internalization by cancer cells beyond their accumulation solely mediated by the debated enhanced permeability and retention (EPR) effect [25–27]. In particular, the use of glucose derivatives as targeting agents is a promising strategy to increase the selectivity of nanoparticles towards tumor cells by leveraging on the peculiar glucose metabolism of cancer known as the Warburg effect [28–30].

Here, we studied the photothermal properties of newly synthesized ultrasmall CDs, emphasizing how nanoscale surface engineering impinge on light–matter interactions and heat generation. By optimizing irradiation parameters, we finely tuned the temperature increase to the mild-hyperthermia window, a regime sensitive to surface energy dissipation pathways. We further introduce a double divergent surface functionalization strategy, decorating CDs with distinct glucose derivatives that differently interact with the GLUT1 transporter, overexpressed in tumor cells [31]. This approach enables a systematic study of how interfacial molecular recognition controls GLUT-mediated cellular internalization of glycosylated CDs. The resulting glycosylated-CDs were also evaluated for their photothermal therapeutic (PTT) efficacy in both 2D and 3D triple-negative breast cancer (mammospheres), as well as non-tumoral cell models. On the whole, we propose a shift in the nanomedicine paradigm by developing a safer, biocompatible, and bioeliminable Trojan horse capable of accumulating in glucose-deprived cancer cells and being locally activated by external light for a more selective and tailored drug-free photothermal therapy of tumors.

2. Materials and methods

2.1. Materials and methods

Citric acid, urea, dimethyl sulfoxide (DMSO), 4-pentynoic acid, poly (ethylene glycol) bis(amine) (Mw=2000), 2-azido-2-deoxy-(D)-glucose, 6-azido-6-deoxy-(D)-glucose, ascorbic acid, copper(II) sulfate, 1-Ethyl-3-(3-dimethyl aminopropyl) carbodiimide hydrochloride (EDC • HCl, 99.5 %), N-hydroxysuccinimide (NHS, 99.5 %), copper sulphate, hydroxypropyl methyl cellulose, SpectraPor® Pre-wetted RC Tubing (MWCO 2 kDa), and SpectraPor® Biotech CE (MWCO 100 – 500 Da) were purchased from Merk Life Science S.r.l. (Milan, Italy). CellTiter 96 AQueous One Solution Cell Proliferation Assay (MTS) was purchased from Promega (Milan, Italy). Dulbecco's modified Eagle's medium (DMEM) with and without phenol red, fetal bovine serum (FBS), L-glutamine, penicillin, streptomycin, and amphotericin B were purchased from EuroClone S.p.A. (Milan, Italy).

Human triple-negative breast cancer cells (MDA-MB-231) were obtained from "Istituto Zooprofilattico Sperimentale della Lombardia e dell'Emilia Romagna", Italy. Human Schwann cells (hTERT ipn02.3 2λ, indicated as HSC) were purchased from ATCC.

2.1.1. Description of characterizations performed

CDs, CDs-2-Glu, and CDs-6-Glu were characterized by FT-IR, DLS, Zeta-potential, ^{1}H NMR, Uv-vis and fluorescence spectroscopy, HR-TEM, EDXS, and AFM. The photothermal kinetics and the photothermal conversion efficacy were obtained in the near infrared (810 nm) over time. The photostability was explored after 20 min of laser exposure. The cytocompatibility, cell uptake, and photothermal ablation of cancer cells were studied on MDA-MB-231 and Schwann cells, used as model of breast cancer cells and glucose-avid normal cells, respectively. All procedures and methods are reported in supporting information.

2.1.2. Statistical analysis

Statistical analysis was performed by one-way analysis of variance (ANOVA) followed by Tukey's post-hoc analysis using the software package GraphPad Prism. Comparisons were considered statistically significant at $p < 0.05$ (*), $p < 0.01$ (**), $p < 0.001$ (***).

3. Results and discussion

CDs were obtained by solvothermal decomposition of citric acid and urea in dimethyl sulfoxide (DMSO), modifying a synthetic route reported elsewhere [32]. The use of DMSO as the reaction solvent marks a fundamental difference from the protocols previously optimized by the research group for the synthesis of CDs [19]. Participating in the reaction as a donor of sulfur atoms, DMSO should contribute with urea to the N/S-co-doping of the carbon nanostructure, which has been associated with enhanced optical properties in the literature [33]. The synthetic protocol effectively led to CDs with an average diameter of ~ 4.0 nm (Fig. 1a-a'). HR-TEM shows the formation of CDs with a monocrystalline β-C_3N_4 structure and hexagonal shape (Fig. 1b), as indicated by the good agreement between its 2-dimensional Fourier transform (FT) and the calculated diffraction pattern of bulk hexagonal β-C_3N_4 (space group P63/m, space group number 176, lattice parameters of $a = b = 6.38$ Å, $c = 2.395$ Å) in the [311] zone axis (Figure 1b').

However, EDXS analysis performed to investigate the chemical composition of CDs excluded a significant presence of S atoms within the nanocrystals (Figure S1), indicating a negligible contribution of DMSO in the formation of CDs, differently from the literature reference, which, however, calculated a low S content in the obtained nanostructures (~ 1.2 %)[32]. Instead, the EDXS analysis revealed the presence of C, N, and O atoms in the structure of CDs, which are arranged in multiple polar functional groups at the CDs' surface. The FT-IR spectrum of CDs presents, indeed, the typical vibration bands of carboxylic and amidic *C = O* stretching (1708 cm^{-1} and 1660 cm^{-1}), O—H (3400 cm^{-1}), aliphatic C—H (2990 cm^{-1}), and C—O stretching (1112 cm^{-1}) (Fig. 1c). Moreover, the spectrum displays a sharp peak at 1385- 1401 cm^{-1} attributable to a peculiar phonon mode associated with C—N stretching vibration within a β-C_3N_4 structure, corroborating HR-TEM results [34]. This rich surface chemistry ensures high dispersibility of CDs in different polar solvents, favoring their processability, and it is valuable for post-synthetic functionalization reactions. The ionizable character of the functional groups described confers a negative Z-potential to the nanoparticles (+28.3 ± 4.2 mV), which is desirable to prevent aggregation phenomena, leading to stable CDs' dispersions over time. As reported in Fig. 1d, CDs present a broad absorption profile extending throughout the UV–Visible region and characterized by several absorption peaks, attributable to π-π* and *n*-π* electronic transitions compatible with the described multifunctional surface [35]. The absorption profile does not undergo significant changes up to 48 h, with no appreciable shift of the main peaks at 450 and 590 nm, and only a slight decrease of absorbance over time. Since any aggregation phenomena are expected to alter the wavelength or intensity of the absorption spectrum, these data indicate that CDs are colloidally stable in aqueous media mimicking physiological conditions obtained by performing the analysis in DMEM without phenol-red and enriched with bovine serum proteins (FBS, 10 % v/v) (pH 7.4) [36].

3.1. Multicolor fluorescence emission of CDs confers self-trackability to the nanosystem

CDs display significant fluorescence emission across a broad spectral range of excitation wavelengths. Interestingly, their emission peak demonstrates a large tunability, clearly visible in Fig. 2a, progressively

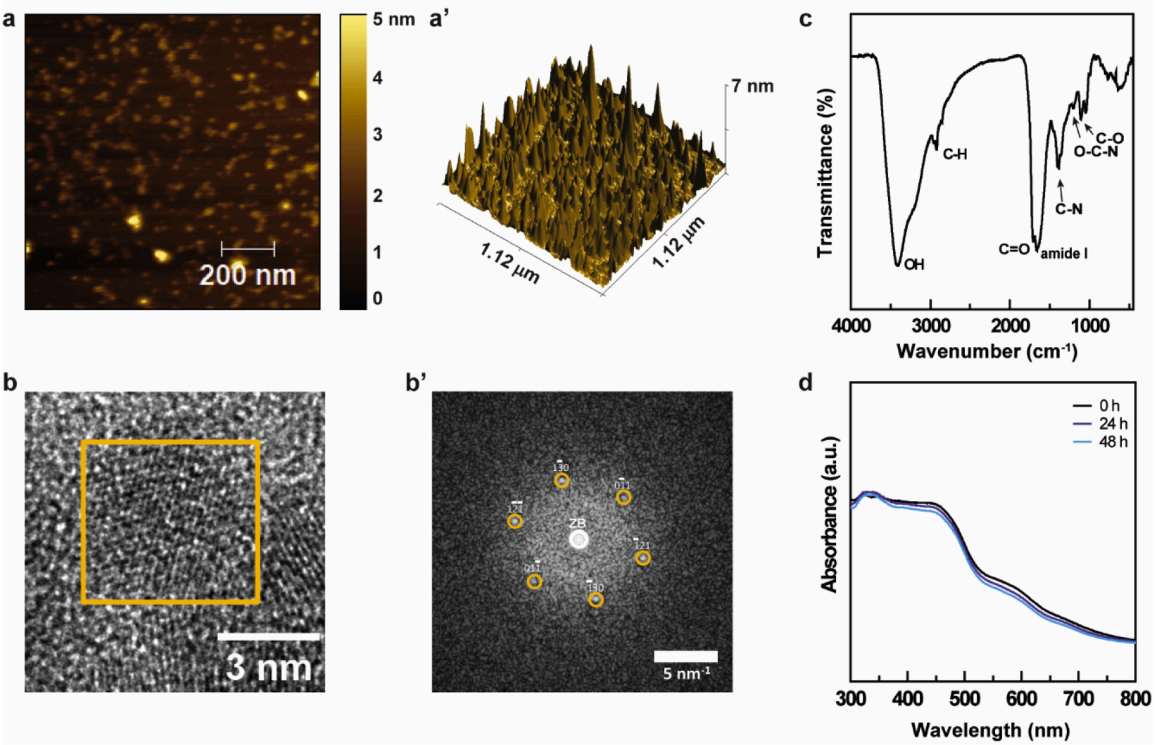

Fig. 1. Characterization of CDs displaying their ultrasmall crystalline nanostructures, their surface chemistry rich in polar functional groups, and high stability in culture medium. Bidimensional (**a**) and tridimensional (**a'**) AFM micrographs of CDs on a mica substrate; HR-TEM image highlighting a single β-C_3N_4 carbon dot (D = 5 nm) within an orange frame (**b**) and its FT pattern (**b'**) together with the calculated diffraction pattern with Miller indices for bulk hexagonal β-C_3N_4 in the [311] zone axis (**b'**); FT-IR spectrum of CDs recorded in the 4000 – 450 cm^{-1} range, with peaks attributions (**c**); UV–Vis absorption spectra of CDs in DMEM without phenol red supplemented with FBS (10 % v/v) recorded at scheduled time intervals (0 h, 24, and 48 h) in the 800 – 300 nm range (**d**).

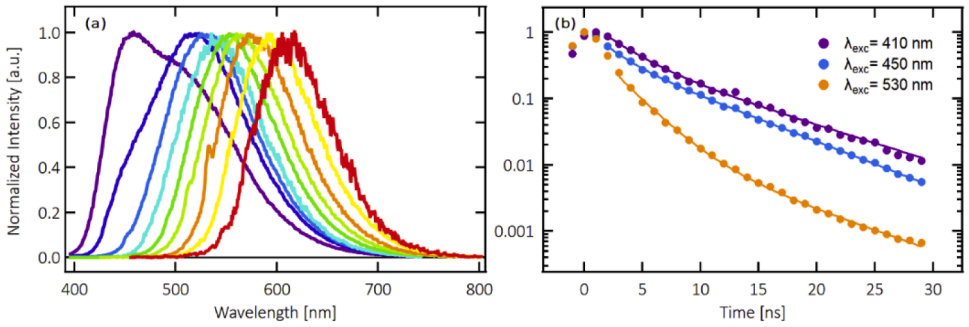

Fig. 2. Characterization of the emission properties of CDs. (a) Normalized fluorescence spectra of CDs under excitation at different wavelengths ranging from 410 nm (violet) to 570 nm (red), with 20 nm increments. (b) Time-resolved decay traces recorded at three representative excitation wavelengths, 410 nm (violet), 450 nm (blue), and 530 nm (orange).

redshifting towards the biologically transparent window, from 500 nm to 610 nm, when the excitation wavelength is tuned from 410 nm to 570 nm. As shown in Fig. 2b, we also carried out time-resolved photoluminescence measurements to determine the excited-state decay properties. These data clearly reveal a multiexponential decay behavior. For example, least-square fitting of the decay trace recorded upon excitation at 410 nm yields two lifetimes of 2.7 ns and 8 ns with relative weights of 56 % and 44 %, respectively. However, the precise values of the lifetimes and their relative weights significantly vary with excitation, as summarized in Table S1.

Indeed, both the emission tunability visible in Fig. 2a and the excitation-dependent multi-exponential decay kinetics are well-known properties of CDs [37,38], ultimately due to the fact that CDs fluorescence stems from a heterogeneous population of chromophores with a statistical distribution of energy gaps and lifetimes. The spectral tunability, in particular, is a useful property for applications as bioimaging, considering it provides degrees of freedom that can be used to select the most advantageous emission properties for applications, for example to efficiently avoid cell auto-fluorescence. Here we exploited the emission properties of CDs to track their cellular internalization by widefield fluorescence microscopy. As shown in Fig. 3, the presence of CDs within both non tumoral (Human Schwann cells, HSC) or breast cancer (MDA-MB-231) was clearly appreciable in DAPI, FITC, and TexasRed channels, as predictable from their multicolor emission profile. After internalization, CDs spread throughout the cells, although the distribution is predominantly cytosolic in non-tumoral cells. The high-resolution micrographs obtained also highlighted the presence of vesicular formations in which CDs were concentrated, as indicted by the brighter fluorescence of these dots; these vesicles are clearly observable in HSC cells, but also present in MDA-MB-231 cells.

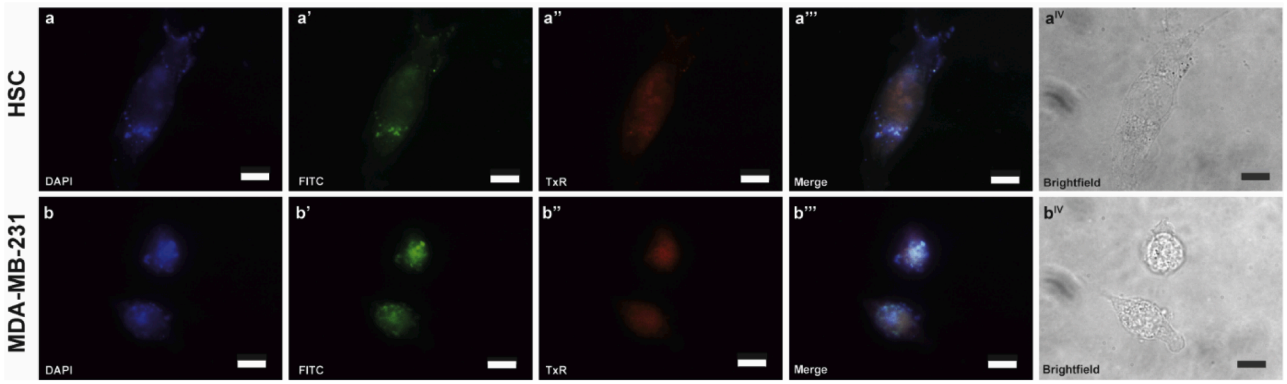

Fig. 3. The self-tracking properties of CDs allow for tracking their cellular internalization by widefield fluorescence microscopy. Micrographs of HSC cells (a-a^{IV}) and MDA-MB-231 cells (b-b^{IV}) acquired in the DAPI (a-b), FITC (a'-b'), Texas-red (TxR, a''-b''), merge (a'''-b'''), and Brightfield (a^{IV}-b^{IV}) channels after 24 h of incubation with CDs (0.5 mg mL^{-1}).

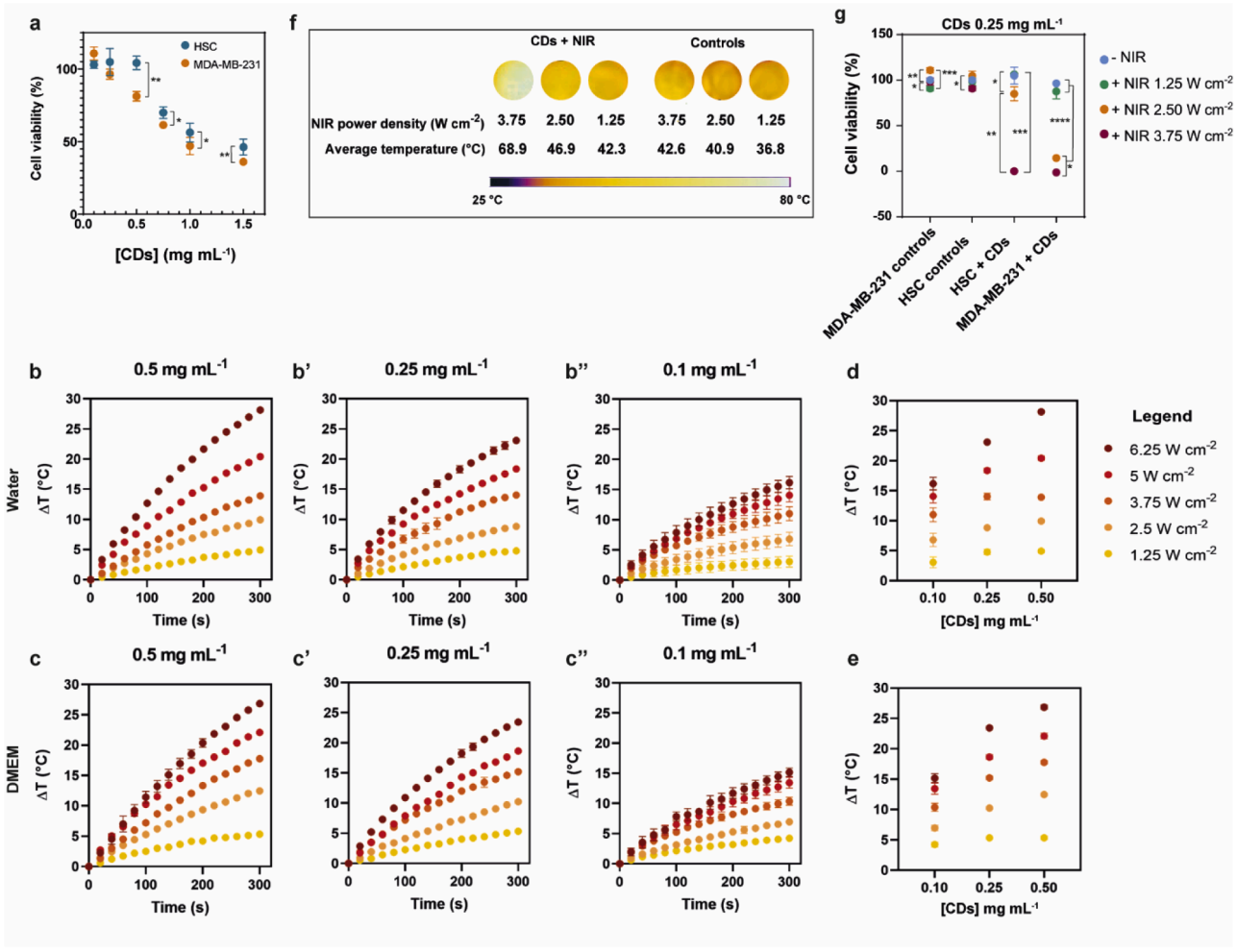

Fig. 4. Modulable photothermal therapy using CDs. Dose-dependent cytotoxicity of CDs on HSC (blue) and MDA-MB-231 (orange) cells highlighting good tolerability of the treatment to relatively high concentrations (**a**), mean ± *S*.D. ($N = 6$); thermal response kinetics of CDs at 0.5 mg mL^{-1} (**b-c**), 0.25 mg mL^{-1} (**b'-c'**), and 0.10 mg mL^{-1} (**b''-c''**) in water (**b-b''**) or DMEM (**c-c''**), under exposure to 1.25 (yellow), 2.5 (light orange), 3.75 (orange), 5 (red), and 6.25 (dark red) W cm^{-2} NIR laser (300 s), mean ± *S*.D. ($N = 3$). Maxima temperatures reached after 300 s irradiation of CDs in water (**d**) or DMEM (**e**), under 1.25 (yellow), 2.5 (light orange), 3.75 (orange), 5 (red), and 6.25 (dark red) W cm^{-2} NIR power density irradiation (300 s). Average temperatures reached in CDs-treated wells (0.25 mg mL^{-1}) exposed to 1.25, 2.5, and 3.75 W cm^{-2} NIR irradiation (300 s) and relative thermographs (**f**). Effect of 1.25 (green), 2.5 (orange), 3.75 (red) W cm^{-2} NIR irradiation (300 s) on cell viability and NIR-triggered cytotoxic effect of CDs (0.25 mg mL^{-1}) exposed to the same laser power densities, on HSC and MDA-MB-231 cells, mean ± *S*.D. ($N = 6$) (**g**).

3.2. Photo-thermal conversion ability of CDs leads to modulable NIR-triggered cytotoxic effects on breast cancer

Following cellular internalization, the CD's core displays a dose-dependent cytotoxic effect with EC_{50} of 1.21 and 0.94 mg mL^{-1} on healthy and breast cancer cell lines respectively, resulting overall well-tolerated up to high concentrations with higher cytocompatibility on healthy cells (Fig. 4a). These data are consistent with the high biocompatibility of CDs reported in the literature, confirming the high safety profile of these nanomaterials [39].

However, the CD's core can be responsible for light-triggered anticancer effects upon near infrared (NIR) laser irradiation as CDs can be also able to convert the absorbed radiative energy into heat, causing a local temperature rise (hyperthermia) that is useful for therapeutic purposes. Thus, we measured the temperature increase (ΔT) produced by increasing concentrations of CDs (0.10, 0.25, and 0.50 mg mL^{-1}), both in water and DMEM, subjected to 300 s of irradiation at different power densities (from 1.25 to 6.25 W cm^{-2}), so as to perform a systematic study of the starting CD's core. Despite the feeble absorbance of CDs in the NIR region, the wavelength of the exciting source was set at 810 nm in order to operate within the biological transparency window, which ensures higher penetration depth looking forward to the translatability potential of the nanosystem [40]. The thermal response kinetics, shown in Fig. 4b–b" and c–c", reveal a progressive increase in ΔT over time at all tested irradiation power densities, clearly evidencing both concentration- and power density–dependent behavior. As shown in Fig. 4d-e, the ΔT obtained after 300 s of irradiation ranges from 3 °C to ~ 28 °C, increasing with CDs concentration and NIR power density, reaching a maximum of ~ 28 °C with the higher concentration and power density, and a minimum of 3 °C at the lower concentration and power density. No critical differences are appreciable between the analysis performed in ultrapure water and DMEM. It might be noticed that the CD's optical core, thanks to the high tunability of the photothermal effect, allows precisely controlled temperature tuning as a function of selected irradiation parameters. This is particularly important because the therapeutic outcome strongly depends on the specific temperature range achieved during the procedure. Thermic treatments reaching mild-hyperthermic conditions (43 – 49 °C) selectively address cancer cells inducing activation of controlled cell death mechanisms and sensitization to concurrent treatments, whereas higher temperatures lead to thermal ablation causing necrosis of targeted tissues [3–5].

The preliminary NIR-triggered cytotoxic effect of CDs was evaluated *In vitro*on triple-negative breast cancer cells and healthy cells. We selected for the study a 0.25 mg mL^{-1} concentration of CDs, which did not lead to cytotoxic effects on both the tested cell lines without irradiation (Fig. 4a), while demonstrating favorable photothermal kinetics. The cell viability study was performed after irradiating both untreated and CDs-treated cells with NIR laser at 1.25, 2.50, and 3.75 W cm^{-2}. According to the preliminary evaluation of CDs' photothermal properties, these selected power densities applied should lead to ~ 5 °C, 10 °C, and 15 °C ΔT, respectively (Figure 4b'-c'), thus increasing the physiological temperature to inoffensive, hyperthermic, and ablative conditions, respectively. Effectively, thermographs acquired during the *In vitro*treatment corroborated the hypothesis, as 3.75 W cm^{-2} irradiation caused a temperature increase up to ~ 70 °C, while 2.5 W cm^{-2} treatment reached hyperthermic conditions of ~ 47 °C, and 1.25 W cm^{-2} irradiation caused only a slight temperature increase as sub-therapeutic levels (~ 42 °C) (Fig. 4f). Coherently with expectations, the photothermal activation of CDs at 3.75 W cm^{-2} led to complete abatement of cell viability on both healthy and cancer cells, whereas the 1.25 W cm^{-2} was harmless on both cell lines (Fig. 4g). The 2.50 W cm^{-2} irradiation caused, instead, a strong reduction in cancer cells viability while maintaining good cytocompatibility on healthy cells, demonstrating a remarkable selective activity. Besides, without nanoparticles treatment, irradiation conditions were innocuous at all tested power densities, corroborating the safety of the NIR laser itself. The ability to finely modulate the photothermal effect to achieve selective anticancer activity highlights CDs as promising optically active cores for further controlled surface engineering with targeting moieties, enabling precision medicine interventions while minimizing damage to healthy tissues.

3.3. Surface functionalization of CDs with glucose-derivatives preserves optical properties

Having demonstrated the outstanding theranostic potential of the developed CD's core, a controlled surface functionalization strategy was investigated to further enhance their selective targeting towards cancer cells through a glucose-mediated mechanism. In particular, the surface engineering of CDs with glucose functions was carefully studied to prevent any reduction of affinity of the glucose derivative with the GLUT1 transporter after conjugation, which should compromise the desired targeting effect. According to kinetic and computational studies reported in the literature, amino acids of GLUT1 transporters interact with the pyran oxygen, and the hydroxyl groups at positions 1, 3, and 4 of glucose in its closed conformation; thus, these binding positions have been excluded for glucose conjugation [41]. In contrast, substitutions of hydroxyl groups at C2 do not impinge on sugar-carrier interaction, leading to the widespread use of 2-deoxy-glucose derivatives for fluorescent cellular labeling, diagnosis, and cancer treatment [42–44]. The hydroxyl at position 6 has a peculiar role as it participates to the hydrogen bonds of glucose with the carrier, but its substitution with O-alkyl chains has been shown to increase rather than decrease the affinity of the sugar with GLUT1, suggesting that hydrophobic interactions within the binding site close to the C6 may contribute to stabilize the glucose interaction [45,46]. Similar enhanced internalization has been described for various C6 glucose-drug conjugates, including anticancer agents [47]. However, despite its potential, the use of C6-glucose derivatives has been little researched, with only a few studies about ^{18}F-labeled 6-fluoro-6-deoxy-D-glucose and glucose-drug conjugates reported in the literature [30]. Therefore, we chose to conjugate glucose to CDs at both position 2 and position 6, thus to evaluate which enantiomer and binding position would lead to higher internalization via GLUT 1-mediated mechanisms and, therefore, to a highly selective cytotoxic effect on triple-negative breast cancer cells. To this aim, CDs were first PEGylated by amide coupling with a hetero bifunctional poly (ethylene glycol) bearing an amine and an alkyne terminal group, which was previously synthesized as described in the SI. This work highlights innovative strategies for surface modification of carbon dots, since the use of heterobifunctional PEG chains coupled with click chemistry approaches allowed high yield monodirectional divergent surface functionalization to avoid CD-CD crosslinking. We particularly selected a discrete 2 kDa PEG chain as spacer for enhancing the stealth properties of the nanosystems, without causing excessive increase of their dimensions, and while providing the needed terminal group for the subsequent click reaction with glucose derivatives [48]. The alkyne terminal function was used to "orthogonally" conjugate CDs with either 2-azido-2-deoxy-(D)-glucose or 6-azido-6-deoxy-(D)-glucose through 1, 3 dipolar Huisgen cycloaddition (Fig. 5).

The proficiency of the synthetic pathway adopted was evaluated both by FT-IR and ^{1}HNMR . In detail, the FT-IR spectrum of CDs-PEG-CC presented the typical bands of C—O-C vibration (1110 cm^{-1}) and C—H aliphatic stretching (2900 cm^{-1}) (Figure S3), attributable to PEG chains, which were bound to CDs by amide coupling, as demonstrated by comparing the carboxylic (1708 cm^{-1}) and amide (I) (1690 cm^{-1}) stretching bands between native and PEGylated CDs. Similar peaks are also appreciable in the FT-IR spectra of CDs-2-Glu and CDs-6-Glu, indicating the presence of the PEG spacer in the conjugates. Compared to unconjugated CDs-PEG-CC, both glycosylated derivatives presented a more defined peak at 1550 cm^{-1} attributable to $C = N$ and $N = N$ stretching, supporting the formation of the 1,2,3-triazole ring following azido-alkyne cycloaddition. Moreover, the glucose-derivatives

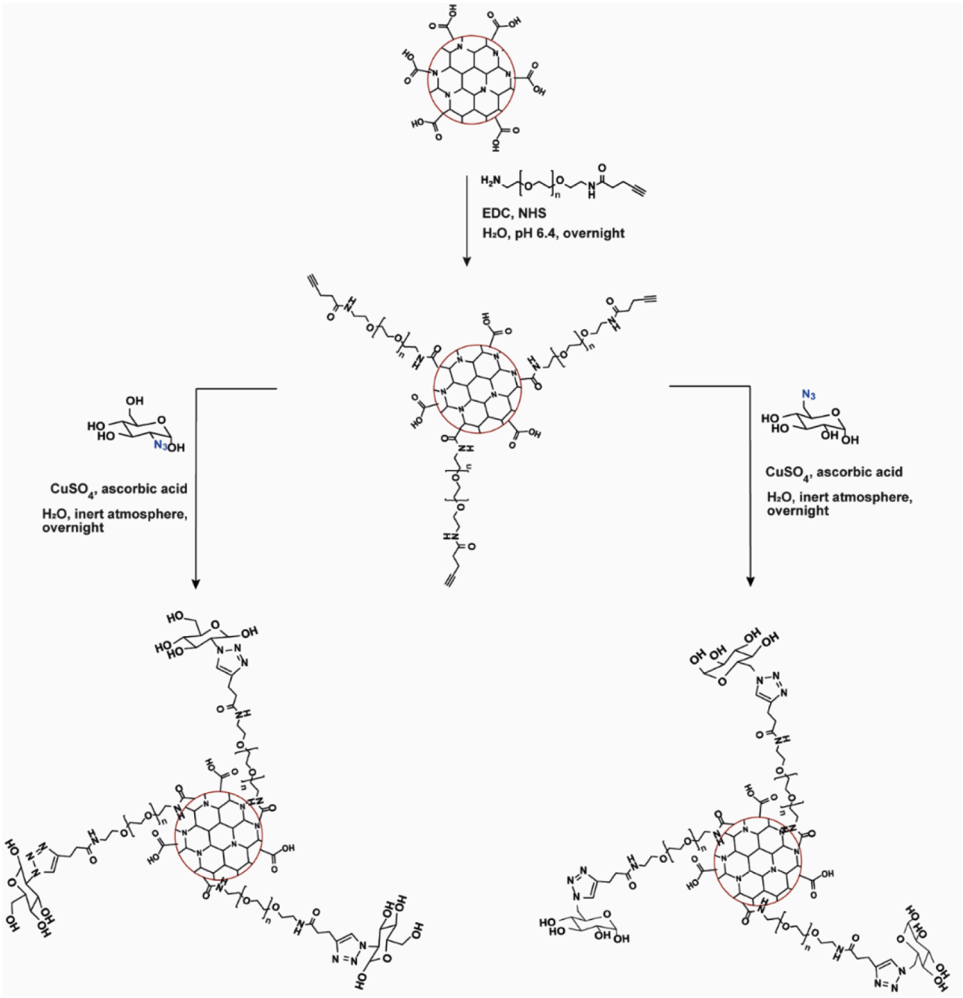

Fig. 5. Synthetic pathway adopted for the surface functionalization of CDs introducing D-glucose as targeting agent. A heterobifunctional PEG was used to functionalize the surface of CDs, providing a biocompatible spacer bearing an alkyne terminal function, which was subsequently exploited to alternatively bind 2-azido-2-deoxy-(D)-glucose or 6-azido-6-deoxy-(D)-glucose through Huisgen cycloaddition.

employed presented an evident peak at 2100 cm^{-1} attributable to the azido group, that was absent in the spectrum of the conjugates,

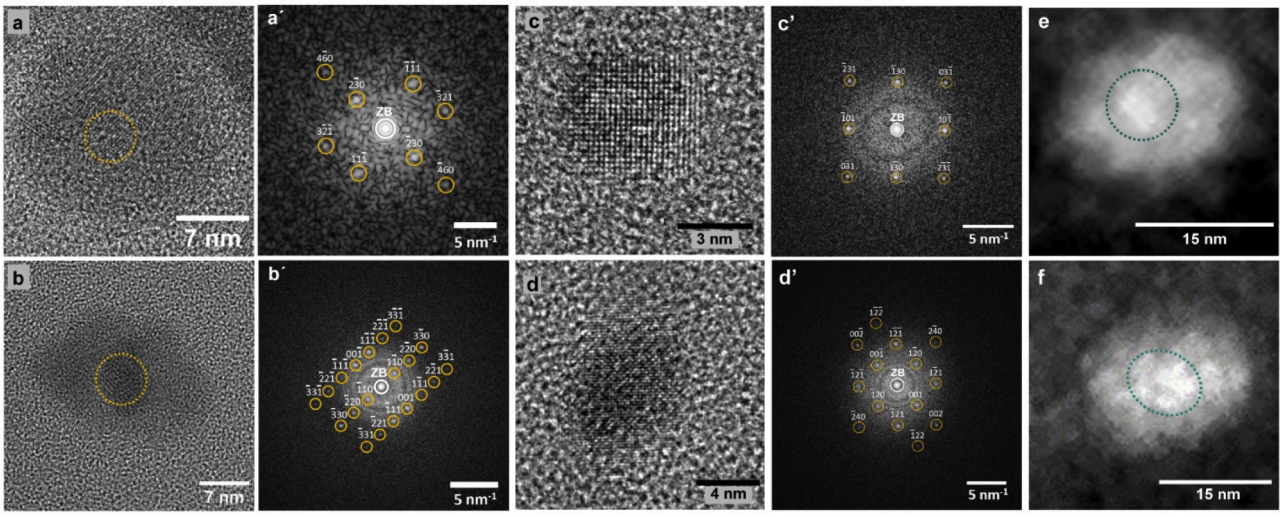

Fig. 6. Structural characterization of CDs-2-Glu and CDs-6-Glu; HR-TEM of CDs-2-Glu (**a**) and CDs-6-Glu (**b**); (**a',b'**) FTs of the core region within the yellow frame in (a) and (b), which agree with the calculated diffraction pattern of bulk hexagonal β-C_3N_4 in [325]- and [110]- zone axis (yellow symbols and Miller indices); HR-TEM micrograph of isolated CDs cores and their FT with calculated diffraction patterns of β-C_3N_4 hexagonal structures in the [313]- and [210]-zone axis for CDs-2-Glu (**c-c'**) and CDs-6-glu (**d-d'**); HAADF STEM micrographs of CDs-2-Glu (**e**) and CDs-6-Glu (**f**); the green circles highlights the slightly bright contrast of the cores.

coherently with the participation of this functional group in the conjugation reaction. Further confirms of the occurred conjugation were obtained by comparing the ^{1}HNMR spectra of the commercial precursors (Figures S4 – S5) to those of CDs-2-Glu and CDs-6-Glu (Figures S6). The spectra of both conjugated presented the typical peaks of D-glucose, which however are shifted if compared to the unconjugated precursor due to the variation of the surrounding chemical environment, together with an additional peak at ~7.9 ppm, compatible with protons of the formed triazole ring. In addition, by adding acetone as internal standard and assuming the density of each particle to be 2.3 g cm^{-2}, we established that the amount of glucose in both samples was similar (3.6 % and 4.2 % for CDs-6-Glu and CDs-2-Glu, respectively). In detail, the structure consists of a CD's core engineered with either 12 or 14 surface PEG chains.

Moreover, differential scanning calorimetry spectra of CDs, CDs-2-Glu, and CDs-6-Glu present different transformations corroborating the formation of new chemical entities after conjugation (Figure S7).

HR-TEM analysis of CDs-2-Glu and CDs-6-Glu displayed nanostructures with a crystalline β-C_3N_4 core of ~ 5 nm, coherently with the presence of CDs as the central element of the conjugates (Fig. 6). HRTEM images clearly show the formation of functionalized β-C_3N_4 dots with sizes of about ≈ 21 nm (CDs-2-Glu on Fig. 6a) or ≈ 25 nm (CDs-6-Glu on Fig. 6b) and β-C_3N_4 monocrystalline cores with D ≈ 5–6 nm (orange frames on Fig. 6a-b), confirmed by their Fourier transformations, which are in agreement with the calculated diffraction pattern of bulk hexagonal β-C_3N_4 in the [325]- and [110]-zone axis, respectively (Fig. 6a'-b'). The formation of 2-Glu/6-Glu shells is shown by the presence of amorphous hollows with a low gray contrast surrounding the β-C_3N_4 cores on HRTEM images of functionalized CDs (Fig. 6a, b). We note that the low contrast of shells on HRTEM images of functionalized CDs is indeed expected, as a consequence of their amorphous structure and the very low mass-thickness contrast related to light atoms forming the shells, i.e. the O, C and N. All these reasons result in an apparent absence of any shell around β-C_3N_4 cores on HRTEM images of many functionalized CDs. However, to demonstrate the formation of functionalized CDs, which apparently did not show any functionalization on their HRTEM images, HRTEM combined with HAADF STEM was used in the following. HRTEM and their corresponding FT are used to the structural characterization of cores for a 2-Glu and a 6-Glu CDs, demonstrating that both cores are monocrystalline with a hexagonal β-C_3N_4 structure in the [313]- and [210]-zone axis, respectively (Fig. 6c-c' and d-d'). Contrary to HRTEM images, where no functionalized shell is visible, their HAADF

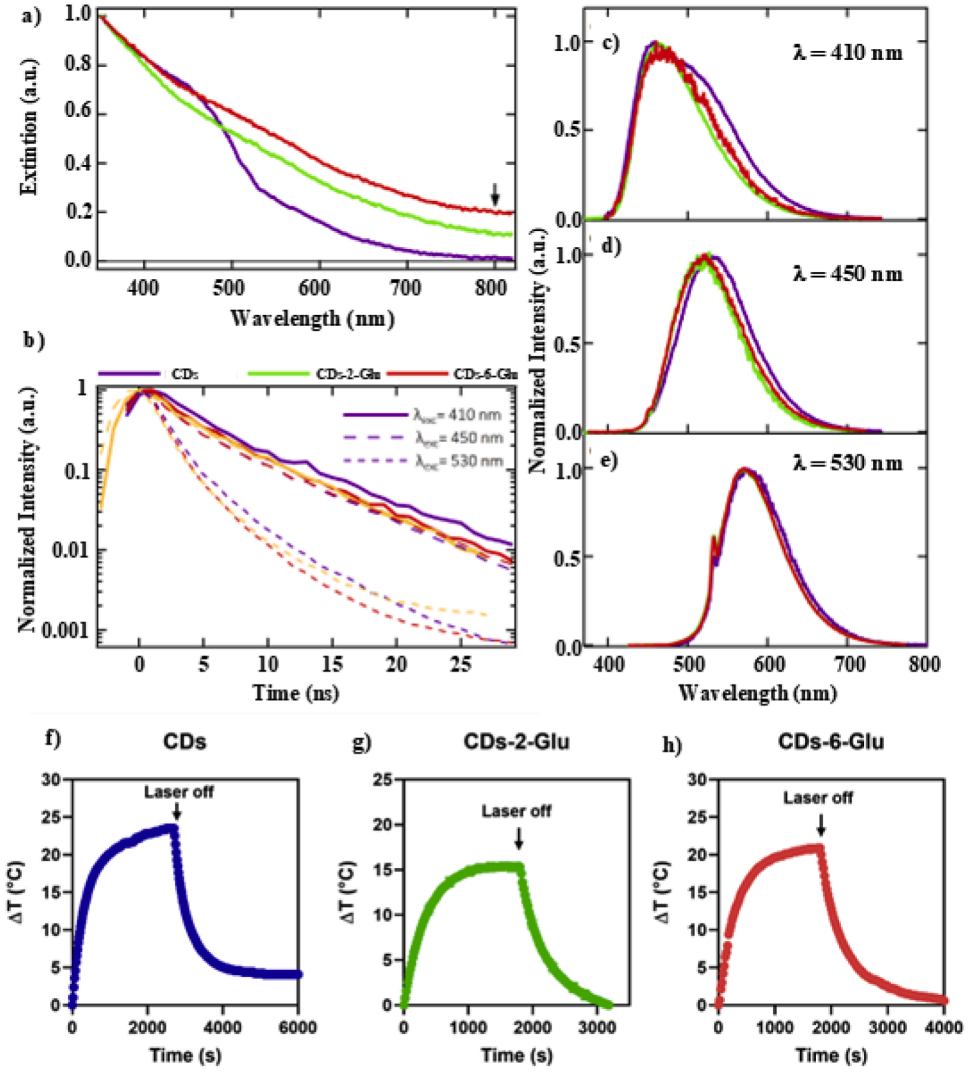

Fig. 7. Optical properties of glycosylated CDs. (a) Normalized absorbance spectra of pristine CDs, CDs-2-Glu and CDs-6-Glu. The arrow highlights the wavelength of 810 nm used for photothermal therapy experiments; (b) Time-resolved PL decay profiles of pristine CDs, CDs-2-Glu, and CDs-6-Glu under excitation at 410 nm (solid lines), 450 nm (dashed lines), and 530 nm (short-dashed lines); (c), (d), (e): Normalized PL spectra of the same three samples under excitation at 410 nm (c), 450 nm (d), and 530 nm (e); In all panels a consistent color scheme is used: purple for pristine CDs, green for CDs-2-Glu, and red for CDs-6-Glu. (f-h) Photothermal conversion experiment obtained for pristine 0.5 mg mL^{-1} aqueous dispersions of CDs, CDs-2-Glu, and CDs-6-Glu under 810 nm 2.5 W cm^{-2}.

STEM images clearly show the formation of shells with thicknesses of ≈ 7–8 nm around the two cores (Fig. 6e,f). Based on their mainly atomic number (Z) contrast, besides the mass-thickness contrast, HAADF STEM images can provide a precise morphological characterization of the obtained glycosylated CDs, corroborating the core-shell structure of single CDs-Glu conjugates. Unfortunately, no clear distinction between the shell and the core of functionalized CDs can be observed on their HAADF STEM images (Fig. 6e,f), because both have about the same Z-contrast being built by the same atoms (i.e. C, O and N). However, the slightly higher density of cores results in a somehow brighter contrast of cores compared with the shell on HAADF STEM images (Fig. 6e,f).

The effect of functionalization on the photophysical properties was systematically compared by absorption, steady-state photoluminescence (PL), and time-resolved fluorescence measurements on pristine CDs and their glycosylated derivatives (CDs-2-Glu and CDs-6-Glu). As shown in Fig. 7a, the UV/VIS spectra of CDs-2-Glu and CDs-6-Glu exhibit a notable variation compared to unconjugated CDs, confirming successful glycosylation. Notably, both conjugates show a significant increase in the observed extinction at around 800 nm, that is critical for PTT applications. While this effect likely arises from enhanced light scattering due to PEGylation (as opposed to enhanced absorption, which is probably negligible), even an increased scattering is expected to enhance the optical path length within biological tissues, thereby improving the efficacy of PTT.

As shown in Fig. 7b-e, the fluorescent properties of glycosilated CDs remain substantially preserved, with negligible changes in the emission bandshapes (Fig. 7c-e) and excited-state lifetimes (see Fig. 7b). In particular, Fig. 7c and d demonstrate that the excitation-dependent tunability of the emission, which is one of the key functional photophysical properties of CDs, is retained upon glucose conjugation. However, we see in Fig. 7c-e a slight emission blue-shift for both CDs-2-Glu and CDs-6-Glu with respect to CDs. This is likely due to the PEG layer on CDs-2-Glu and CDs-6-Glu providing chromophores on CD surfaces with a partial shielding from solvation interactions [49]. Therefore, this effect further confirms the successful functionalization of CDs' surfaces via the glycosylation process. Finally, absolute quantum yield (QY) measurements with λ_{exc} = 450 nm were performed on all three nanosystems using an integrating sphere, revealing a QY of ~ 1 %. Although this value would generally be considered as too low for purely optical applications, it is still sufficient for bioimaging and cellular tracking, as confirmed in the following. Indeed, such a relatively low QY is suitable for bioimaging applications, as showed below in cell uptake studies, and advantageous for PTT applications, as it implies the dominance of efficient non-radiative pathways, which are essential for efficient heat generation upon light irradiation. The non-radiative predominance of the CDs-2-Glu and CDs-6-Glu conjugates is clearly shown in Fig. 7f-h, in comparison with the pristine CDs, where it is possible to see a sharp photothermal behavior of all samples, with a photothermal conversion efficiency calculated to be 35 and 37, respectively. These values are slightly lower than the pristine CDs (41 %), mainly due to the PEG-Glu shell, but comparable to that observed for graphene-based (58 %) nanosystems and gold nanorods (~56 %) [50,51]. Not surprisingly, the photothermal kinetics showed a power-dependent trend for both conjugates (Figure S8), suggesting that the local hyperthermia can be modulated as a function of the time exposure and power settled.

3.4. GLUT-mediated internalization of CDs-2-Glu and CDs-6-Glu

The uptake of CDs-2-Glu, CDs-6-Glu, and CDs by cancer and healthy cells was evaluated on tridimensional cultures of MDA-MB-231 and HSC cells. HSC cells were selected as a non-tumoral cell line due to their known expression of GLUT1 receptors [52], making them an appropriate control model for our study.

To establish whether developed nanosystems were internalized by cells via a glucose-dependent mechanism, the analysis was performed inhibiting GLUT membran proteins that are involved in the internalization of glucose by cells. This was achieved by adding a known GLUT inhibitor, (GLUTi, BAY-876, 2 μM). The red self-fluorescence of CDs was exploited to track their internalization by widefield fluorescence microscopy and micrographs, reported in Fig. 8a-c, were analyzed with the ImageJ software to quantify the area-normalized mean fluorescence intensity (MFI, a.u.). As shown in Fig. 8d, unconjugated CDs entered both MDA-MB-231 and HSC cells through a mechanism that does not depend on GLUT inhibition, besides displaying a preferential uptake by cancer cells. After glycosylation, nanoparticles maintained their ability to enter non-cancerous cells similarly to unconjugated CDs, with no significant differences in the presence of the GLUTi (Figure 8d'-d''). GLUT inhibition caused, instead, a remarkable reduction of MFI in MDA-MB-231 3D-cultures treated with CDs-2-Glu and CDs-6-Glu, indicating a glucose-mediated internalization mechanism in breast cancer cells for both glycosylated CDs. Notably, mammospheres treated with CDs-6-Glu (Figure 8d″) displayed red fluorescence levels two-fold higher of those observed with the CDs-2-Glu conjugate (Figure 8d'). Moreover, the functionalization of CDs with D-glucose in position 2 resulted inefficient in favoring breast cancer targeting, presenting similar uptake by cancerous and non-cancerous cell cultures overexpressing GLUT1 receptors. While, CDs-6-Glu demonstrated a higher cellular uptake in MDA-MB-231 compared to healthy HSCs, indicating that functionalization in position 6 is preferable for achieving active targeting. By employing a divergent glycosylation strategy, we provide new insight into how clever surface engineering of CDs with glucose derivatives regulate transporter-mediated nanoparticle recognition and internalization at the cell–nanomedicine interface. Unlike conventional nanoparticles (50–200 nm in diameter) that rely primarily on enhanced accumulation, this study advances a mechanistic understanding of surface-driven cellular uptake by demonstrating that a divergent functionalization strategy, avoiding particle-particle crosslinking, preserves the ultrasmall dimensions of the CDs, enabling effective exposure of surface glucose moieties, reduced steric hindrance, and enhanced diffusivity at the bio–nano interface, thereby promoting GLUT1-mediated transport.

3.5. NIR-induced cytotoxic effect of CDs-2-Glu and CDs-6-Glu

Both glycosylated CDs maintained a high cytocompatibility on both MDA-MB-231 and HSC cells, with half-maximal effective concentrations (EC_{50}) above 1.0 mg mL^{-1} (Fig. 9a), although showing a slight but significant reduction of cancer cell viability at the higher concentration tested, coherently with a selective cellular uptake (Fig. 9b).

Considering the interesting anticancer effect achieved with 300 s NIR-irradiation of CDs at 2.5 W cm^{-2} power density, the same conditions were applied to evaluate the NIR-triggered cytotoxic effect of CDs-2-Glu and CD-6-Glu at increasing concentrations. Results, reported in Figure 8b', displayed a dose-dependent cytotoxic effect of both CDs-glucose conjugates on healthy and cancer cells, even though with critical differences. In detail, the NIR activation of CDs-2-Glu caused significant reductions in cell viability only at the higher concentration tested (0.25 mg mL^{-1}), which was enhanced towards breast cancer cells (26 % cell viability) compared to healthy cells (57 % cell viability). At the same concentration, CDs-6-Glu caused complete abatement of cell viability of both MDA-MB-231 and HSC cells, resembling conditions of thermal ablation and demonstrating a higher cytotoxic profile. Effectively, thermographs acquired to measure the temperature reached in the culture well after 300 s of NIR irradiation confirm that CDs-6-Glu caused a higher temperature increase compared to CDs-2-Glu (54 °C vs 48.2 °C) (Fig. 9c), thus explaining the different cytotoxicity profile. Besides, CDs-6-Glu were effective in inducing a selective antitumoral effect already at 0.1 mg mL^{-1}, leading to 65 % cell viability of MDA-MB-231 compared to the negligible reduction of cell viability of healthy cells. Since CDs-2-Glu and CDs-6-Glu activated by NIR irradiation induce similar temperature increase in the culture well at 0.1 mg mL^{-1}, both reaching ~ 46 °C, the higher selectivity of CDs-6-Glu is not

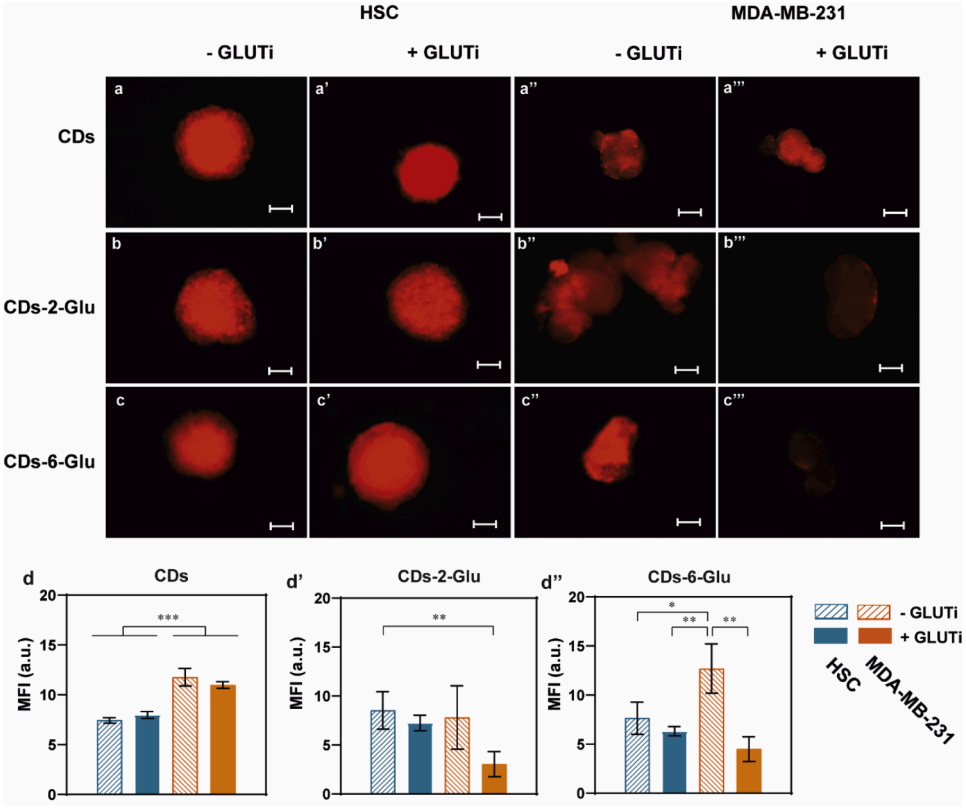

Fig. 8. GLUT-mediated internalization of CDs-2-Glu and CDs-6-Glu. Micrographs were obtained using the TexasRed optical filter and a 5 X magnification. The red self-fluorescence of CDs (a-a'''), CDs-2-Glu (b-b'''), and CDs-6-Glu (c-c''') was exploited to evaluate their internalization within 3D-cultures of HSC (a-b-c, a'-b'-c') and MDA-MB-231 (a''- b''-c'', a'''-b'''-c'''). The analysis was performed without (a-b-c, a''-b''-c'') and with (a'-b'-c', a'''-b'''-c''') GLUT inhibition. Scalebar = 100 μm; area-normalized mean fluorescence intensity (MFI) of HSC (blue) and MDA-MB-231 (orange) cells treated with CDs (**d**), CDs-2-Glu (**d'**), or CDs-6-Glu (**d''**); analysis was performed with (full) or without (empty lined) pretreatment with GLUTi, mean ± *S*.D. ($N = 6$).

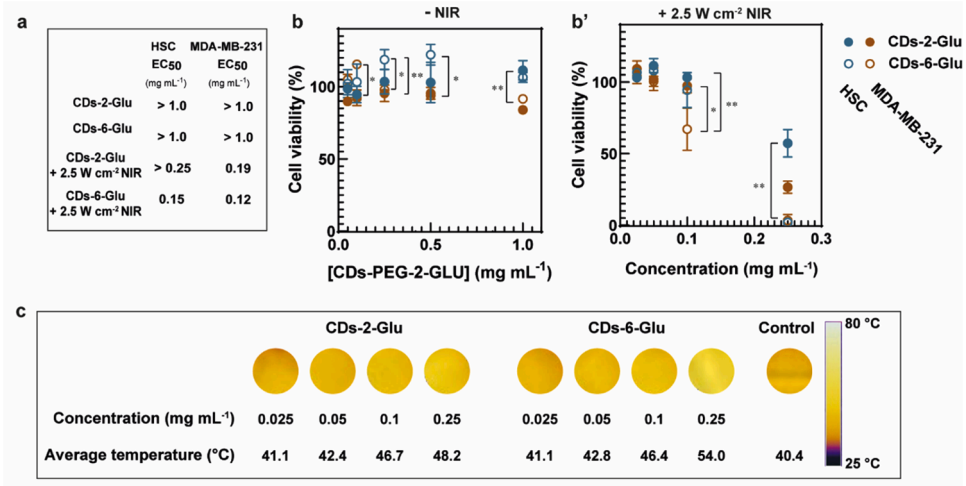

Fig. 9. NIR-induced cytotoxic effect of CDs-2-Glu and CDs-6-Glu; Table reporting half-maximal effective concentration (EC_{50}) values for CDS-2-Glu and CDs-6-Glu, with and without 2.5 W cm^{-2} NIR laser, on HSC and MDA-MB-231 cells (**a**). Cell viability study of HSC (blue) and MDA-MB-231 (orange) cells, treated with CDs-2-Glu (full dots) or CDs-6-Glu (empty dots) at concentrations comprised in the 0.1 – 1.0 mg mL^{-1} range (**b**), mean ± *S*.D. ($N = 6$); NIR-triggered cytotoxic effect of CDs-2-Glu (full dots) or CDs-6-Glu (empty dots) (2.5×10^{-2} - 2.5×10^{-1} mg mL^{-1}) on HSC (blue) and MDA-MB-231 (orange) cells (**b'**) irradiated with NIR at 2.5 W cm^{-2}, 300 s. Thermographs of cell culture wells treated with CDs-2-Glu or CDs-6-Glu (2.5×10^{-2} - 2.5×10^{-1} mg mL^{-1}) and NIR-irradiation (2.5 W cm^{-2}, 300 s) or only NIR irradiation (Control), and calculated average temperature reached after the treatment (**c**).

ascribable to the temperature reached. Rather, CDs-6-Glu display more efficient antitumoral effect at low-doses because of the different internalization pathways compared to CDs-2-Glu, which result in enhanced effectiveness of the hyperthermic treatment. Therefore, between the functionalization strategies proposed, CDs binding to glucose in position 6 provided more promising results.

Focusing on CDs-6-Glu, in a subsequent experimental set we evaluated the tunability of their NIR-triggered cytotoxic effect, testing lower

power densities of irradiation (1.25 and 0.5 W cm^{-2} power densities) and higher NPs concentration (0.25, 0.5, and 0.75 mg mL^{-1}). Results, reported in Figure S9, indicate that changing the operative parameters it was possible to modulate the cytotoxicity of the treatment, obtaining controllable therapeutic effects.

Comprehensively, glycosylated CDs demonstrated their efficacy as theranostic nanosystems for NIR-triggered photothermal therapy of breast cancer, and CDs-6-Glu in particular proved enhanced internalization by cancer cells and low-dose NIR-induced anticancer properties, leading to extremely tailorable antitumoral effects.

4. Conclusions

We successfully synthetized biocompatible red-emitting carbon dots (CDs) of 4 nm in diameter, with hexagonal carbon nitride (β-C_3N_4) crystalline structure amenable to versatile surface functionalization with targeting agents. The obtained CDs showed noteworthy optical properties, including a tunable multicolor fluorescence emission with multiexponential decay behavior, and remarkable photothermal conversion efficiency (~40 %). While their emission properties conferred self-trackability to CDs, enabling monitoring their intracellular localization in both non-tumoral and breast cancer cells, their ability to convert light into heat was exploited to perform thermal treatments. We engineered the surface of CDs with 2-deoxy-(D)-glucose or 6-deoxy-(D)-glucose as targeting agents, obtaining a neat core-shell structure of reduced dimension (20 nm in diameter). The controlled divergent functionalization with glucose moieties was attained by using heterobifunctional PEG linkers carrying one amine group and one alkyne function as end chains, which implies orthogonal reactivity between the CD's surface and the azido function of glucose. The conjugation caused a variation of CDs' optical properties, resulting in enhanced extinction at ~ 800 nm, while preserving tunable fluorescence emission. Besides, QY analysis revealed the prevalence of non-radiative relaxation pathways after excitation, valuable for PTT application. Effectively, cytotoxicity studies corroborated the extremely controllable photothermal properties of glycosylated CDs enabling highly precise antitumoral effects though fine-tuning of the treatment temperature. *In vitro* studies on 3D models of MDA-MB-231 and HSC cells also demonstrated the proficiency of the targeting strategy adopted, resulting in glucose-mediated uptake of glycosylated CDs on breast cancer cells. Between CDs-2-Glu and CDs-6-Glu, the second also exhibits a preferential uptake in breast cancer cells and enhanced NIR-triggered antitumoral effect at lower doses, indicating as most promising the conjugation with D-glucose in position 6. Even though further in-depth characterization on more complex biological models is required, our study provided interesting insights for developing highly tumor-selective nanoplatforms, underscoring the exceptional potential of glycosylated CDs as theranostic nanosystems to perform precision breast cancer therapy.

Funding sources

G.C. and N.M.: The research leading to these results has received funding from the European Union – NextGenerationEU through the Italian Ministry of University and Research under PNRR - M4C2-I1.3 Project PE_00000019: "Health Extended ALliance for Innovative Therapies, Advanced Lab-research, and Integrated Approaches of Precision Medicine – HEAL ITALIA" . CUP: B73C22001250006. The views and opinions expressed are those of the authors only and do not necessarily reflect those of the European Union or the European Commission. Neither the European Union nor the European Commission can be held responsible for them.

CRediT authorship contribution statement

Roberta Cillari: Writing – review & editing, Writing – original draft, Methodology, Investigation, Formal analysis, Data curation. **Alice Sciortino:** Writing – review & editing, Resources, Methodology, Investigation, Formal analysis, Data curation. **Radian Popescu:** Writing – review & editing, Methodology, Data curation. **Riccardo Rubino:** Writing – review & editing, Methodology, Formal analysis, Data curation. **Yolita M. Eggeler:** Writing – review & editing, Resources. **Marco Cannas:** Writing – review & editing, Resources. **Fabrizio Messina:** Writing – review & editing, Supervision, Resources, Methodology, Investigation. **Gennara Cavallaro:** Writing – review & editing, Resources. **Nicolò Mauro:** Writing – review & editing, Writing – original draft, Supervision, Resources, Investigation, Conceptualization.

Declaration of competing interest

The authors declare that they have no known competing financial interests or personal relationships that could have appeared to influence the work reported in this paper.

Acknowledgement

Roberta Cillari was supported by Fondazione Umberto Veronesi under the supervision of N. M.

Supplementary materials

Supplementary material associated with this article can be found, in the online version, at doi:10.1016/j.surfin.2026.108792.

Data availability

Data will be made available on request.

References

[1] H. Sun, Q. Zhang, J. Li, S. Peng, X. Wang, R. Cai, Near-infrared photoactivated nanomedicines for photothermal synergistic cancer therapy, Nano Today 37 (2021) 101073, https://doi.org/10.1016/j.nantod.2020.101073.
[2] L. Zhao, X. Zhang, X. Wang, X. Guan, W. Zhang, J. Ma, Recent advances in selective photothermal therapy of tumor, J. Nanobiotechnology. 19 (2021) 1–15, https://doi.org/10.1186/S12951-021-01080-3/FIGURES/7.
[3] J.L. Roti, Cellular responses to hyperthermia (40–46 °C): cell killing and molecular events, Int. J. Hyperthermia 24 (2008) 3–15, https://doi.org/10.1080/02656730701769841.
[4] M. Dunne, M. Regenold, C. Allen, Hyperthermia can alter tumor physiology and improve chemo- and radio-therapy efficacy, Adv. Drug Deliv. Rev. 163–164 (2020) 98–124, https://doi.org/10.1016/J.ADDR.2020.07.007.
[5] C. Brace, Thermal tumor ablation in clinical use, IEEe Pulse 2 (2011) 28–38, https://doi.org/10.1109/MPUL.2011.942603.
[6] A. Bettaieb, P.K. Wrzal, D.A. Averill-Bates, A. Bettaieb, P.K. Wrzal, D.A. Averill-Bates, Hyperthermia: cancer treatment and beyond, Can. Treat. - Convent. Innov. Approach. (2013), https://doi.org/10.5772/55795.
[7] P.R. Stauffer, Evolving technology for thermal therapy of cancer, Int. J. Hyperthermia, Taylor and Francis Ltd. (2005) 731–744, https://doi.org/10.1080/02656730500331868.
[8] X. Li, J.F. Lovell, J. Yoon, X. Chen, Clinical development and potential of photothermal and photodynamic therapies for cancer, Nat. Rev. Clin. Oncol. 17 (2020) 657–674, https://doi.org/10.1038/s41571-020-0410-2, 11 17.
[9] S.G. Alamdari, M. Amini, N. Jalilzadeh, B. Baradaran, R. Mohammadzadeh, A. Mokhtarzadeh, F. Oroojalian, Recent advances in nanoparticle-based photothermal therapy for breast cancer, J. Controll. Release 349 (2022) 269–303, https://doi.org/10.1016/J.JCONREL.2022.06.050.
[10] Y. Song, X. Tong, Y. Han, Q.W. Zhang, Finely tunable NIR-II organic scaffolds for fluorescence/photoacoustic duplex imaging–guided noninvasive photothermal therapy of glioblastoma, Aggregate 6 (2024) e680, https://doi.org/10.1002/AGT2.680;WEBSITE:WEBSITE:PERICLES;REQUESTEDJOURNAL:JOURNAL:26924560;JOURNAL:JOURNAL:26924560;WGROUP:STRING:PUBLICATION.
[11] A.K. Parchur, G. Sharma, J.M. Jagtap, V.R. Gogineni, P.S. Laviolette, M.J. Flister, S. B. White, A. Joshi, Vascular Interventional radiology-guided photothermal therapy of colorectal cancer liver metastasis with theranostic gold nanorods, ACS. Nano 12 (2018) 6597–6611, https://doi.org/10.1021/ACSNANO.8B01424/ASSET/IMAGES/LARGE/NN-2018-01424J_0009.JPEG.
[12] X. Pei, J. Wang, Q. Wan, Comment on "amine-modified graphene: thrombo-protective safer alternative to graphene oxide for biomedical applications, ACS. Nano 8 (2014) 1966, https://doi.org/10.1021/NN5000578.
[13] Y. Zhao, T. Zhao, Y. Cao, J. Sun, Q. Zhou, H. Chen, S. Guo, Y. Wang, Y. Zhen, X. J. Liang, S. Zhang, Temperature-sensitive lipid-coated carbon nanotubes for synergistic photothermal therapy and gene therapy, ACS. Nano 15 (2021)

6517–6529, https://doi.org/10.1021/ACSNANO.0C08790/ASSET/IMAGES/MEDIUM/NN0C08790_M001.GIF.
[14] Y. Zhang, L. Wang, L. Liu, L. Lin, F. Liu, Z. Xie, H. Tian, X. Chen, Engineering metal-organic frameworks for photoacoustic imaging-guided chemo-/photothermal combinational tumor therapy, ACS. Appl. Mater. Interfaces. 10 (2018) 41035–41045, https://doi.org/10.1021/ACSAMI.8B13492/ASSET/IMAGES/LARGE/AM-2018-13492X_0006.JPEG.
[15] N. Mauro, R. Cillari, C. Gagliardo, M.A. Utzeri, M. Marrale, G. Cavallaro, Gadolinium-doped carbon nanodots as potential anticancer tools for multimodal image-guided photothermal therapy and tumor monitoring, ACS. Appl. Nano Mater. 6 (2023), https://doi.org/10.1021/acsanm.3c03583.
[16] B. Geng, D. Yang, D. Pan, L. Wang, F. Zheng, W. Shen, C. Zhang, X. Li, NIR-responsive carbon dots for efficient photothermal cancer therapy at low power densities, Carbon. N. Y. 134 (2018) 153–162, https://doi.org/10.1016/J.CARBON.2018.03.084.
[17] O.U. Akakuru, J. Xing, S. Huang, Z.M. Iqbal, S. Bryant, A. Wu, M. Trifkovic, Leveraging non-radiative transitions in Asphaltenes-derived carbon dots for cancer photothermal therapy, Small. 21 (2025) 2404591, https://doi.org/10.1002/SMLL.202404591.
[18] G. Roscigno, A. Affinito, C. Quintavalle, R. Cillari, G. Condorelli, G. Cavallaro, N. Mauro, Ultrasmall carbon nanodots as theranostic nanoheaters for Precision Breast cancer phototherapy: establishing the translational potential in tumor-in-a-dish models, ACS. Biomater. Sci. Eng. 10 (2024) 4269–4278, https://doi.org/10.1021/acsbiomaterials.4c00209.
[19] N. Mauro, M.A. Utzeri, A. Sciortino, F. Messina, M. Cannas, R. Popescu, D. Gerthsen, G. Buscarino, G. Cavallaro, G. Giammona, Decagram-scale synthesis of multicolor carbon nanodots: self-tracking nanoheaters with inherent and selective anticancer properties, ACS. Appl. Mater. Interfaces. 14 (2022) 2551–2563, https://doi.org/10.1021/ACSAMI.1C19599/ASSET/IMAGES/LARGE/AM1C19599_0006.JPEG.
[20] R. Cillari, R.C. Acúrcio, A. Barateiro, H.F. Florindo, N. Mauro, G. Cavallaro, Harnessing sulfur-doped carbon nanodots conjugated with IDO inhibitors act as a dual-mode breast cancer immunotherapy, J. Controll. Release 381 (2025) 113575, https://doi.org/10.1016/J.JCONREL.2025.02.071.
[21] X. He, Z. Wang, B. Wang, Y. Zhang, X. Xu, H. Cai, S. Lu, Recent advances in carbon dots imaging at the subcellular level: synthesis strategies, properties, and organelle imaging, Chin. Chem. Lett. 37 (2026) 111957, https://doi.org/10.1016/j.cclet.2025.111957.
[22] R. Jelinek, Characterization and physical properties of carbon-dots, Carbon Nanostruct. 0 (2017) 29–46, https://doi.org/10.1007/978-3-319-43911-2_3.
[23] J. Yoo, C. Park, G. Yi, D. Lee, H. Koo, Active targeting strategies using biological ligands for nanoparticle drug delivery systems, Cancers. (Basel) 11 (2019) 640, https://doi.org/10.3390/cancers11050640.
[24] M.F. Attia, N. Anton, J. Wallyn, Z. Omran, T.F. Vandamme, An overview of active and passive targeting strategies to improve the nanocarriers efficiency to tumour sites, J. Pharm. Pharmacol. 71 (2019) 1185–1198, https://doi.org/10.1111/JPHP.13098.
[25] J.W. Nichols, Y.H. Bae, EPR: evidence and fallacy, J. Controll. Release 190 (2014) 451–464, https://doi.org/10.1016/J.JCONREL.2014.03.057.
[26] R. Sun, J. Xiang, Q. Zhou, Y. Piao, J. Tang, S. Shao, Z. Zhou, Y.H. Bae, Y. Shen, The tumor EPR effect for cancer drug delivery: current status, limitations, and alternatives, Adv. Drug Deliv. Rev. 191 (2022) 114614, https://doi.org/10.1016/J.ADDR.2022.114614.
[27] F. Danhier, To exploit the tumor microenvironment: since the EPR effect fails in the clinic, what is the future of nanomedicine? J. Controll. Release 244 (2016) 108–121, https://doi.org/10.1016/J.JCONREL.2016.11.015.
[28] R. Cillari, S. Scirè, G. Cavallaro, N. Mauro, Ultrasmall glucose-functionalized Au-carbon nanohybrids: exploiting the Warburg effect to image tumors by Multimodal CT/fluorescence imaging, C 2024, Vol. 10, Page 35 10 (2024) 35. https://doi.org/10.3390/C10020035.
[29] Y. Li, W. Hong, H. Zhang, T.T. Zhang, Z. Chen, S. Yuan, P. Peng, M. Xiao, L. Xu, Photothermally triggered cytosolic drug delivery of glucose functionalized polydopamine nanoparticles in response to tumor microenvironment for the GLUT1-targeting chemo-phototherapy, J. Controll. Release 317 (2020) 232–245, https://doi.org/10.1016/J.JCONREL.2019.11.031.
[30] E.C. Calvaresi, P.J. Hergenrother, Glucose conjugation for the specific targeting and treatment of cancer, Chem. Sci. 4 (2013) 2319–2333, https://doi.org/10.1039/C3SC22205E.
[31] J. Wang, C. Ye, C. Chen, H. Xiong, B. Xie, J. Zhou, Y. Chen, S. Zheng, L. Wang, Glucose transporter GLUT1 expression and clinical outcome in solid tumors: a systematic review and meta-analysis, 2017. www.impactjournals.com/oncotarget/.
[32] X. Bao, Y. Yuan, J. Chen, B. Zhang, D. Li, D. Zhou, P. Jing, G. Xu, Y. Wang, K. Holá, D. Shen, C. Wu, L. Song, C. Liu, R. Zbořil, S. Qu, In vivo theranostics with near-infrared-emitting carbon dots—Highly efficient photothermal therapy based on passive targeting after intravenous administration, Light: Sci. Appl. 7 (2018) 1–11, https://doi.org/10.1038/s41377-018-0090-1, 1 7.
[33] F. Yan, Z. Sun, H. Zhang, X. Sun, Y. Jiang, Z. Bai, The fluorescence mechanism of carbon dots, and methods for tuning their emission color: a review, Microchimica Acta 186 (2019), https://doi.org/10.1007/s00604-019-3688-y.
[34] F. Messina, L. Sciortino, R. Popescu, A.M. Venezia, A. Sciortino, G. Buscarino, S. Agnello, R. Schneider, D. Gerthsen, M. Cannas, F.M. Gelardi, Fluorescent nitrogen-rich carbon nanodots with an unexpected β-C3N4 nanocrystalline structure, J. Mater. Chem. C. Mater. 4 (2016) 2598–2605, https://doi.org/10.1039/C5TC04096E.
[35] Y. Park, J. Yoo, B. Lim, W. Kwon, S.W. Rhee, Improving the functionality of carbon nanodots: doping and surface functionalization, J. Mater. Chem. a Mater. 4 (2016) 11582–11603, https://doi.org/10.1039/c6ta04813g.
[36] P. Bélteky, A. Rónavári, N. Igaz, B. Szerencsés, I.Y. Tóth, I. Pfeiffer, M. Kiricsi, Z. Kónya, Silver nanoparticles: aggregation behavior in biorelevant conditions and its impact on biological activity, Int. J. Nanomedicine 14 (2019) 667–687, https://doi.org/10.2147/IJN.S185965.
[37] J. Guo, P. Zhang, L. Zhu, H. Chen, H.X. Shen, C.F. Wang, S. Chen, Solvent-engineered synthesis of multicolor emissive carbon dots from citric acid and cyanamide, Ind. Eng. Chem. Res. 63 (2024) 9050–9057, https://doi.org/10.1021/ACS.IECR.4C00136/ASSET/IMAGES/LARGE/IE4C00136_0005.JPEG.
[38] A. Sciortino, A. Cannizzo, F. Messina, Carbon nanodots: a review-from the current understanding of the fundamental photophysics to the full control of the optical response, (2018). https://doi.org/10.3390/c4040067.
[39] Y. Choi, S. Kim, M.-H. Choi, S.-R. Ryoo, J. Park, D.-H. Min, B.-S. Kim, Highly biocompatible carbon nanodots for simultaneous bioimaging and targeted photodynamic therapy In vitro and In vivo, Adv. Funct. Mater. 24 (2014) 5781–5789, https://doi.org/10.1002/adfm.201400961.
[40] C.-L. Tsai, J.-C. Chen, W.-J. Wang, Near-infrared absorption property of biological soft tissue constituents, J. Med. Biol. Eng. 21 (2001) 7–14.
[41] M. Mueckler, C. Makepeace, Model of the exofacial substrate-binding site and helical folding of the human Glut1 glucose transporter based on scanning mutagenesis, Biochemistry 48 (2009) 5934–5942, https://doi.org/10.1021/BI900521N/ASSET/IMAGES/LARGE/BI-2009-00521N_0005.JPEG.
[42] J.J.M. Van Der Hoeven, N.C. Krak, O.S. Hoekstra, E.F.I. Comans, R.P.A. Boom, D. Van Geldere, S. Meijer, E. Van Der Wall, J. Buter, H.M. Pinedo, G.J.J. Teule, A. A. Lammertsma, 18F-2-fluoro-2-deoxy-D-glucose positron emission tomography in staging of locally advanced breast cancer, J. Clin. Oncol. 22 (2004) 1253–1259, https://doi.org/10.1200/JCO.2004.07.058.
[43] S.R. Millon, J.H. Ostrander, J.Q. Brown, A. Raheja, V.L. Seewaldt, N. Ramanujam, Uptake of 2-NBDG as a method to monitor therapy response in breast cancer cell lines, Breast. Cancer Res. Treat. 126 (2011) 55–62, https://doi.org/10.1007/S10549-010-0884-1.
[44] X. Jiang, H. Xin, Q. Ren, J. Gu, L. Zhu, F. Du, C. Feng, Y. Xie, X. Sha, X. Fang, Nanoparticles of 2-deoxy-D-glucose functionalized poly(ethylene glycol)-co-poly (trimethylene carbonate) for dual-targeted drug delivery in glioma treatment, Biomaterials 35 (2014) 518–529, https://doi.org/10.1016/J.BIOMATERIALS.2013.09.094.
[45] J.E. Barnett, G.D. Holman, K.A. Munday, Structural requirements for binding to the sugar-transport system of the human erythrocyte, Biochem. J. 131 (1973) 211, https://doi.org/10.1042/BJ1310211.
[46] T. Halmos, M. Santarromana, K. Antonakis, D. Scherman, Synthesis of glucose-chlorambucil derivatives and their recognition by the human GLUT1 glucose transporter, Eur. J. Pharmacol. 318 (1996) 477–484, https://doi.org/10.1016/S0014-2999(96)00796-0.
[47] M. Domińska, G. Pastuch-Gawołek, M. Skonieczna, W. Szeja, A. Domiński, P. Kurcok, Glycoconjugation of quinoline derivatives using the C-6 position in sugars as a strategy for improving the selectivity and cytotoxicity of functionalized compounds, Molecules. 27 (2022) 6918, https://doi.org/10.3390/MOLECULES27206918/S1.
[48] D.E. Owens, N.A. Peppas, Opsonization, biodistribution, and pharmacokinetics of polymeric nanoparticles, Int. J. Pharm. 307 (2006) 93–102, https://doi.org/10.1016/J.IJPHARM.2005.10.010.
[49] Z. Peng, C. Ji, Y. Zhou, T. Zhao, R.M. Leblanc, Polyethylene glycol (PEG) derived carbon dots: preparation and applications, Appl. Mater. Today 20 (2020) 100677, https://doi.org/10.1016/j.apmt.2020.100677.
[50] P. Magnani, P. Varghese Cherian, G.W. Gould, D.A. Greene, A.A.F. Sima, F. C. Brosius, Glucose transporters in rat peripheral nerve: paranodal expression of GLUT1 and GLUT3, Metabolism. 45 (1996) 1466–1473, https://doi.org/10.1016/S0026-0495(96)90174-2.